Industrial benchmark simulations of detached flows using XFlow

M. Chávez-Modena[*], E. Ferrer[*], J.L. Martínez[†], and J.A. Cabello[†]

[*]Universidad Politécnica de Madrid - ETSIAE
Pz. Cardenal Cisneros 3, E28040 Madrid Spain,
m.chavez@upm.es
[†]Future projects, Airbus Spain
Paseo John Lennon, E28906 Madrid Spain.

Abstract

We present simulations of turbulent detached flows using the commercial lattice-Boltzmann solver, XFlow. Using traditional Computation Fluid Dynamics (CFD) software, industrial problems require time consuming meshing processes. Due to its particle-based methodology, the meshing complexity is reduced in XFlow, allowing to solve complex geometries easily using octree structures. However, this ease for meshing rises the question of accuracy to compute detached flows. The performance of XFlow will be demonstrated for different industrial benchmarks and compared to experimental data.

We select four industrial cases: first, the Goldschmied Body[10] at Re= $8.9 \cdot 10^4$. Second, the HLWP-2 (2nd High-Lift Prediction Workshop)[19] geometry, which represents a full aircraft at Re= $1.35 \cdot 10^6$ and Re= $15.1 \cdot 10^6$. Third, a dynamic stall for a NACA0012[15] at Re= $0.98 \cdot 10^6$ for a reduced frequency, $k = 0.1$. Finally, a parametric study to improve wing stall using tubercles located at the leading edge at Re/$L = 4.66 \cdot 10^6$ with a reference length, L.

1. Introduction

Traditional Computation Fluid Dynamics (CFD) have been employed for decades in industry and strong simulation processes have been already established based on Navier-Stokes (N-S) solvers. These solvers face limitations especially related to the mesh and geometry, to model moving geometries with complex motions, or when strongly unsteady and separated flows are involved. Serious alternative to finite volumes and elements methods are now available, among them the lattice-Boltzmann method (LBM) is considered a promising methodology to address these limitations. To illustrate the ability of the LBM to solve industrial problems with detached flows, XFlow is applied to compute four industrial applications: the Goldschmied Body,[10] the HLWP-2 (2nd High-Lift Prediction Workshop),[19] a dynamic stall for a NACA0012[15] and a wing with leading-edge tubercles.[16]

The aerodynamics performance is an important part of the design process of an aircraft. The aeronautical industry have been using CFD as an important complement to the wind tunnel measurements, normally executed at the end of the production cycle. The CFD studies present the strong advantage to allow several design iterations before the manufacturing of the actual product and therefore lowers the manufacturing costs drastically. The analysis of an aircraft relies on its aerodynamic performance in linear regime, i.e. within reasonable incidence angles. However, another critical design feature relies on the ability of an aircraft to maintain its aerodynamics performance up to high angles of attack, in order to enhance stability and safety. This involves mostly aircraft in high-lift configurations used for landing and take-off, where the aircraft can reach high angles of incidence to proceed in the maneuver. This so-called stall prediction analysis consists in capturing the angle of incidence after which the boundary layer separates on most of the aircraft wing, and consequently loses lift.

Nowadays the N-S solvers are able to predict with high accuracy the linear aerodynamic performances, however they face strong difficulties and limitations when predicting stall. There are multiple reasons: first of all the wing geometry of an aircraft in high-lift configuration is complex since the flap and slat are deflected, and thus it is extremely difficult to mesh in the gap between the wing and the flap or slat. Furthermore the flow is highly separated and unsteady due to the large separation regions, and standard turbulence models tend to fail in predicting correct flow separation in such conditions. These two reasons make the solution convergence difficult or even impossible in most cases.

The aim of this work is to test the LBM capabilities to predict detached flows in different industrial application. The content of this text is organized as follows. First, Section 2 introduces the LBM with the different models implemented in XFlow. Section 3 describes various applications, XFlow setup and numerical results. Finally, Section 4 summarizes the main conclusions of the work.

2. Numerical methodology

2.1 Lattice-Boltzmann Method

The lattice-Boltzmann Method relies on the Boltzmann transport equation applied to probability distribution functions (PDF), f, to describe the fluid behavior at mesoscopic scale. The method consists of a straightforward collision-streaming scheme that resolves the discrete Boltzmann transport equation:

$$f_i(\mathbf{x} + \mathbf{e_i}\Delta t, t + \Delta t) - f_i(\mathbf{x}, t) = \Delta t \Omega_i(\mathbf{x}, t), \quad i = 0, ..., Q - 1, \tag{1}$$

where f_i is the PDF in the direction i, Q is the number of velocity directions, $\mathbf{x}$ is the position vector, $\mathbf{e_i}$ is the discrete velocity direction vector and Ω_i is the collision operator. The first two terms are calling streaming steps while the right hand side is called collision operator.

The streaming step model describes the transport of the particle distribution functions along discrete directions, while most of the physical phenomena are modeled by the collision operator, which also has a strong impact on the numerical stability of the scheme. The stream-and-collide scheme is executed over a lattice, which consists of a Cartesian points distribution with a discrete set of velocity directions. The lattice scheme is usually denoted as DnQm where n represents the dimension of the problem, and m the number of velocity directions. The most common lattice schemes are the D2Q9 or D3Q19. However XFlow is a LBM solver based on the D3Q27 lattice scheme which provides more discrete velocities and symmetries.

The macroscopic variables are recovered through the calculation of the statistical moments, $\mu_{x^k y^l z^m}$, defined by the following relation:

$$\mu_{x^k y^l z^m} = \sum_{i=1}^{Q} f_i e_{ix}^k e_{iy}^l e_{iz}^m, \tag{2}$$

where k, l, and m are respectively the orders of the moments taken in x, y, and z directions respectively. The moment order is therefore $k + l + m$. For instance, the moment of order zero provides the density, and the moment of order one provides the momentum:

$$\mu_{x^0 y^0 y^0} = \sum_{i=1}^{Q} f_i = \rho, \quad \mu_{x^1 y^0 y^0} = \sum_{i=1}^{Q} f_i \mathbf{e}_{ix} = \rho \mathbf{u}. \tag{3}$$

2.1.1 Octree lattice structure

The lattice structure featured by XFlow is the D3Q27 organized as an octree structure. The octree structure offers the possibility to use a non-uniform lattice structure, and therefore have different spatial scales at different locations of the fluid domain.

XFlow pre-processor generates the initial octree lattice structure based on the input geometries, the user-specified lattice resolution for each geometry, as well as the farfield resolution. User-defined regions (sphere, box, cylinder, etc.) can also be created to refine arbitrary regions at the specified lattice resolution. The different spatial scales employed are hierarchically arranged. Each level solves spatial and temporal scales twice smaller than the previous level, thus forming the aforementioned octree structure (see Figure 1). This is particularly efficient as the ratio $\Delta x / \Delta t$ is maintained in the entire fluid domain, thus ensuring a constant CFL condition and speed of sound at any location of the fluid domain. Finite volume and finite element methods normally use a global time step which is inefficient for the coarser mesh cells, whereas the local time step approach in XFlow allows to have always an adapted time step for every lattice size of your fluid domain.

This initial lattice structure can be modified during the simulations by the XFlow solver based on several criteria. First, if the computational domain changes due to presence of moving geometries, the lattice can dynamically be refined to follow the new position of the geometry every time step. Other adaptive refinement criteria to adapt the flow physics are also available. A refinement algorithm based on the level of vorticity is effective to dynamically refine the wake region (Figure 1), characterized by high vorticity.
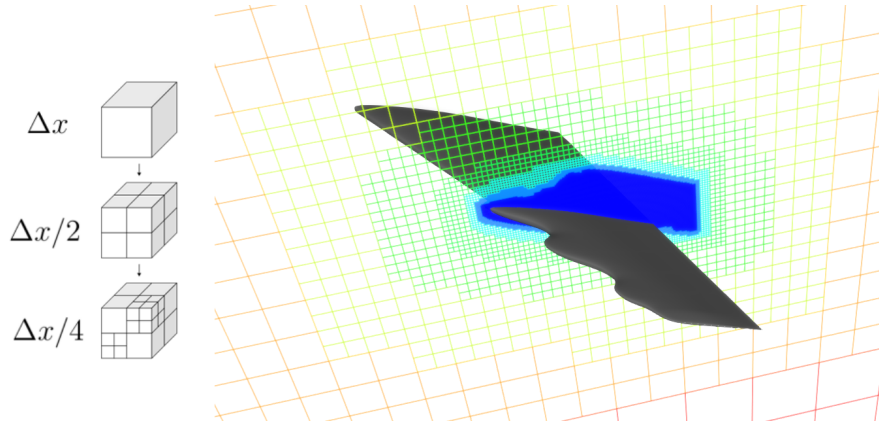
Figure 1: Octree lattice structure with different lattice resolution.

2.1.2 Collision operator

The collision operator, also called scattering operator, relaxes the system to an equilibrium state. The single-relaxation time based on the Bhatnagar-Gross-Krook (BGK)[2] approximation is the most popular approach. The BGK collision operator, is still common but has several limitations for high Reynolds number flows.[11]

The multiple-relaxation time with raw moments (MRT-RM) was developed in an attempt to overcome some of the limitations of the BGK.[5] This method performs the collision process in momentum space instead of in velocity space. The increased flexibility in the selection of the relaxation parameters with respect to the BGK approach resulted in an enhanced stability when compared with the BGK.[14] Despite its increased stability, the MRT-RM still shows instabilities for small viscosities,[9] due to the lack of Galilean invariance. The multiple-relaxation time with central moments (MRT-CM) improved some of the shortcomings of the MRT-RM by calculating the moments with respect to a local velocity.[8,9] By shifting the discrete velocities with the local macroscopic velocity, it is possible to obtain a higher degree of Galilean invariance compared with the MRT-RM approach. The expressions for the three collisions operators are:

$$\Omega_i^{\text{BGK}} = \frac{1}{\tau}(f_i^{\text{eq}} - f_i), \quad \Omega_{f_j}^{\text{MRT-RM}} = M_{jk}(0)^{-1} S_{kl} M_{li}(0)(f_i^{\text{eq}} - f_i), \quad \Omega_{f_j}^{\text{MRT-CM}} = M_{jk}(\mathbf{u})^{-1} S_{kl} M_{li}(\mathbf{u})(f_i^{\text{eq}} - f_i), \qquad (4)$$

where τ is the relaxation time, f_i^{eq} is the local equilibrium function, M_{ij} is the transformation moment matrix and S_{ij} is the diagonal relaxation matrix.

Whereas most of the LBM collision operators are based on the BGK approximation, XFlow uses a MRT collision operator implemented in central-moment space which benefits of a low numerical dissipation even for low viscosity and strongly improves symmetries in the scheme.[9,17] This implementation allows especially to reach higher Mach and Reynolds numbers than the BGK approximation.

2.2 Turbulence Modeling

The approach used for turbulence modeling is the Large Eddy Simulation (LES) technique. This scheme introduces an additional viscosity, called turbulent eddy viscosity ν_t, in order to model the under-resolved subgrid turbulence. The LES model used in XFlow is the Wall-Adapting Local Eddy (WALE) viscosity model, that provides a consistent local eddy-viscosity and near wall behavior.[6]

INDUSTRIAL BENCHMARK SIMULATIONS OF DETACHED FLOWS USING XFLOW

The actual implementation is formulated as follows:

$$\nu_t = \Delta_f^2 \frac{(G_{\alpha\beta}^d G_{\alpha\beta}^d)^{3/2}}{(S_{\alpha\beta}S_{\alpha\beta})^{5/2} + (G_{\alpha\beta}^d G_{\alpha\beta}^d)^{5/4}},$$

$$S_{\alpha\beta} = \frac{g_{\alpha\beta} + g_{\beta\alpha}}{2},$$

$$G_{\alpha\beta}^d = \frac{1}{2}(g_{\alpha\beta}^2 + g_{\beta\alpha}^2) - \frac{1}{3}\delta_{\alpha\beta}g_{\gamma\gamma}^2, \quad (5)$$

$$g_{\alpha\beta} = \frac{\partial u_\alpha}{\partial x_\beta},$$

where $\Delta_f = C_w \Delta x$ is the filter scale, S is the strain rate tensor of the resolved scales and the constant C_w is typically 0.325.

The strain rate tensor, $g_{\alpha\beta}$, is locally available with the LBM as the second-order moment, which makes extremely efficient the implementation of state-of-the-art LES models.

Furthermore, the Cartesian lattice structure is well suited for LES turbulence models. Because of the isotropic nature of turbulence out of the boundary layer, the LES turbulence model require cells with proportioned aspect ratio. The lattice completely fulfills this requirement.

2.3 Near-Wall Treatment

In addition to the LES turbulence modeling, XFlow uses wall function in order to model the near-wall region and boundary layer, and therefore employs the so-called Wall-Modeled LES approach (WMLES). The isotropy of the lattice structure would imply an unreasonably high number of elements to resolve the boundary layer. This issue is addressed by the use of a generalized law of the wall.

The boudary layer is modeled by a generalized law of wall given by Shih et al.[21] based on a previous work of Tennekes and Lumley.[22] The approach takes into account the effect of adverse and favorable pressure gradients described in Eq. 6.
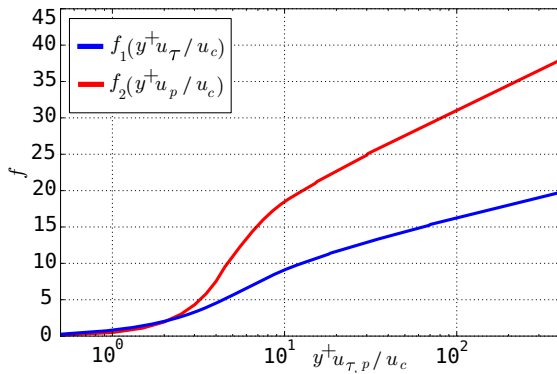

$$\frac{U}{u_c} = \frac{U_1 + U_2}{u_c} = \frac{u_\tau}{u_c}\frac{U_1}{u_\tau} + \frac{u_p}{u_c}\frac{U_2}{u_p}$$

$$= \frac{\tau_w}{\rho u_\tau^2}\frac{u_\tau}{u_c}f_1\left(y^+\frac{u_\tau}{u_c}\right) + \frac{dp_w/dx}{|dp_w/dx|}\frac{u_p}{u_c}f_2\left(y^+\frac{u_p}{u_c}\right),$$

$$y^+ = \frac{u_c y}{\nu}, \quad (6)$$

$$u_c = u_\tau + u_p,$$

$$u_\tau = \sqrt{|\tau_w|/\rho},$$

$$u_p = \left(\frac{\nu}{\rho}\left|\frac{dp_w}{dx}\right|\right)^{1/3},$$

Figure 2: Unified laws of the wall.

where y is the normal distance from the wall, x is the local flow direction tangentially to the wall, u_τ is the skin friction velocity, τ_w is the turbulent wall shear stress, dp_w/dx is the wall pressure gradient, u_p is a characteristic velocity of the adverse wall pressure gradient and U is the mean velocity at a given distance from the wall. The interpolating functions f_1 and f_2 are depicted in Figure 2. The velocity field of the boundary layer is obtained through the y^+ which depends on the distance between the first lattice from the geometry wall, y, and the velocity of this first lattice, u_c.

XFlow projects the set of discrete velocities on the geometry tessellation to obtain the wall distance and thus discretize the geometry as depicted Figure 3. This implies a high level of details for the geometry discretization as one lattice node can detect up to 27 geometry projections. These projected velocities are also used to calculate the curvature of the surface that is taken into account for the wall function.

2.3.1 Advanced dynamic geometries

The flexibility of the octree lattice structure and the advanced near-wall treatment proposed by XFlow allows to address one of the most important difficulties faced by the traditional CFD: the fluid-structure interaction. XFlow proposes two
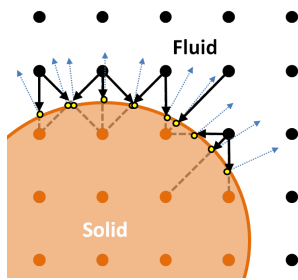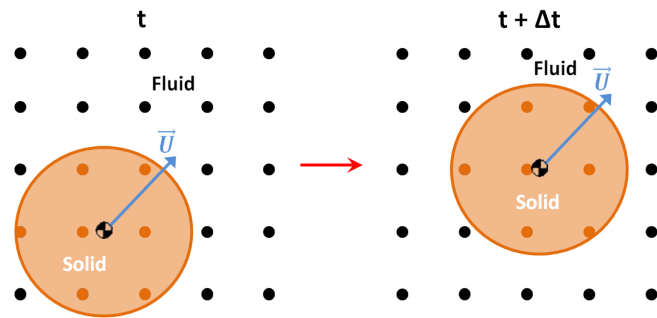
Figure 3: Wall distance and curvature calculation.

Figure 4: Lattice nodes identification in moving geometry process.

different options to handle dynamic geometries: the enforced behavior, and the rigid body dynamics behavior. The enforced behavior moves a geometry based on an input position and orientation law, enforcing the motion of the object. The rigid body dynamics behavior couples the fluid equations resolved by the XFlow that handles rigid bodies allowing up to 6 degrees of freedom.

For both dynamic behaviors, the lattice structure is updated every time step to mark the lattice nodes that belong to the fluid region, and those that belong to solid region as depicted Figure 4. The discrete velocities are also projected every time step in order to compute the new distance to the wall required for the wall function.

On the other hand, the rotating geometry can be addressed with an immersed boundary method. This method replaces broken links with a modified LBM collision operator, solving the time consuming and pressure fluctuations produced by the standard XFlow approach. It works by computing the solid-covered fraction of the volume associated with each lattice site. This computation is a simple lookup, no need for expensive triangle lookups. LBM takes into account the collision with the given solid fraction at each site includes XFlow's law-of-the-wall, allowing for accurate determination of slip velocity and skin friction.

3. Simulations

3.1 Goldschmied Body

3.1.1   Introduction

The selfpropulsing fuselage concept was introduced by F. R. Goldschmied in the 50's[10] showing promise in reducing drag and increasing the aerodynamic efficiency of bullet shape fuselages (see Figure 5). Namely, Goldschmied introduced the idea of including an almost passive flow control strategy to force the flow to remain attached, hence reducing drag. To control separation a fan is installed within the body tail and induces a pressure deficit. It is capable to force the flow to remain attached even in presence of strong adverse pressure gradients induced by the body geometry. The challenge for XFlow is to predict correctly the detached flow with different pressure gradients produced by the fan.
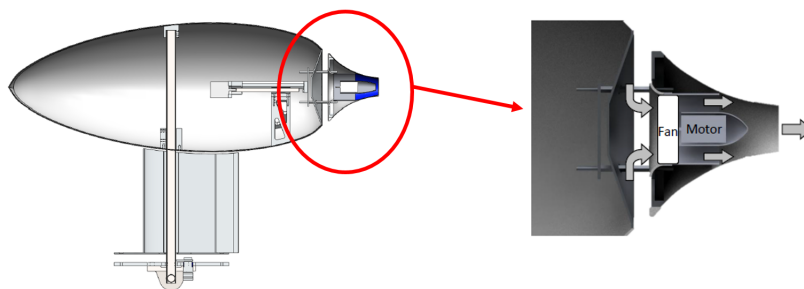

Figure 5: Goldschmied geometry model (Figure 25 in Thomason's work[23]).

3.1.2 Setup and mesh convergence

The model was created from the Thomason's work.[23] It was tested in a wind tunnel with the following dimensions: 12m long, 1.22m wide and 0.9m height. Free slip boundary condition has been used at the lateral walls. Velocity inlet boundary condition was used at the inlet and convective pressure outlet at the outlet. For the Goldschmied's wall, the boundary condition of non-equilibrium enhanced wall function was imposed to take into account pressure gradients in the separation prediction. The fan boundary condition was imposed through a pressure gradient, ΔP. To simulate this case, a single phase external flow set up with the isothermal model has been selected. In addition, the turbulence model, Wall-Adapting Local Eddy-viscosity (WALE), has been used.

The reference velocity and length used to compute aerodynamic coefficients are $U_\infty = 0.2$ and $S_{ref} = 0.2402 m^2$ (frontal surface is used). The resulting Reynolds number for this case is Re $= 9 \cdot 10^4$.

In reference to the grid dependency, three different grid sizes for the zero pressure gradient condition, ΔP = 0Pa, have been computed as shown Table 1. The drag coefficient, Cd, values converge towards the experimental value when the refinement increases. Therefore, the Fine grid has been used for the following simulations because it has a better agreement between the simulations and experimental values. An adaptive grid refinement in function of the vorticity field has been used during the computations.

Table 1: Resolution dependency at ΔP = 0Pa.

	Lattice resolution (mm)	Elements	Simulation time (s)	Cd	Comp. time (h)	Cores [*]
Coarse	4	$1.3 \cdot 10^6$	0.5	0.24	3.2	16
Medium	2	$6.5 \cdot 10^6$	0.5	0.091	10	32
Fine	1.5	$30.3 \cdot 10^6$	0.5	0.066	25	64
Experimental	-	-	-	0.055	-	-

[*] CeSViMA: Supercomputing and Visualization Center of Madrid.

3.1.3 Results

Additionally to the Cd comparison shown in Table 1, Figure 6 shows the pressure coefficient distribution and surface flow pattern for both pressure gradient condition, ΔP = 0Pa and 500Pa, with the finest grid. When comparing these distributions against experimental values it appears that the numerical solution predicts accurately the detached flow position. At ΔP = 0Pa condition, the detached position occurs slightly before the experimental, however the pressure drop level is well predicted. On the other hand, at ΔP = 500Pa, the pressure coefficient is slightly over predicted, however the detachment flow point is well captured.

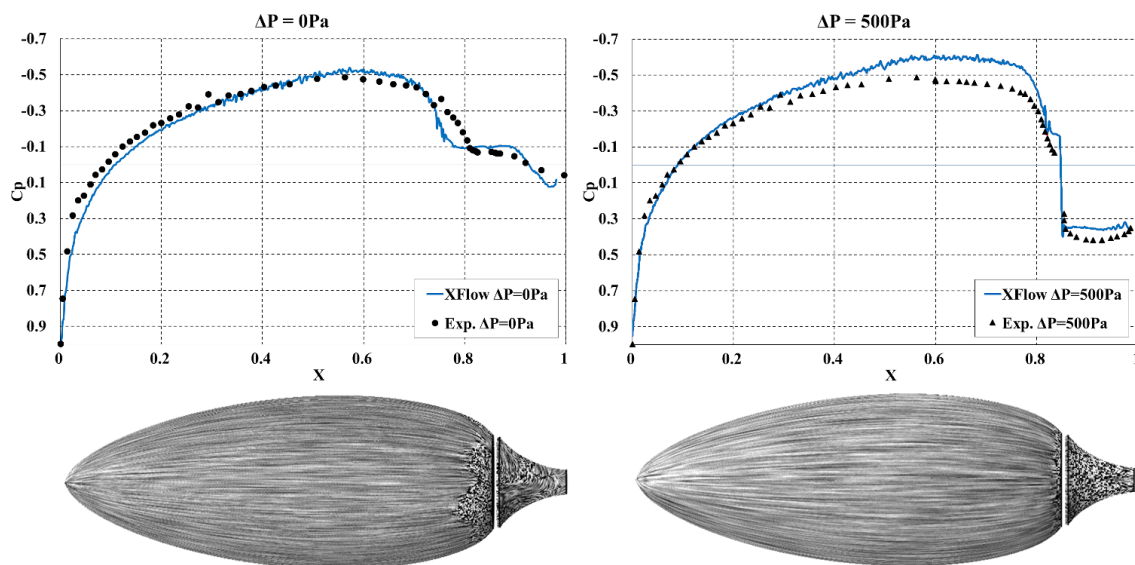Figure 6: Cp distribution (top) and surface flow pattern (bottom) with ΔP = 0Pa (left) and ΔP = 500Pa (right) at Re=8.9 $\cdot 10^4$ (based on the body length).

3.2 2nd High-Lift Prediction Workshop

3.2.1 Introduction

The 2nd High-Lift Prediction Workshop (HiLiftPW-2)[12, 19] provides a benchmark to study linear and post-stall regions on a high-lift aircraft configuration. The DLR F11 geometry includes geometrical details such as slat tracks, flap track fairings and slat pressure tube bundles, which introduce complexity when generating the mesh.

This section contains part of the results published by Brionnaud et al.[12] with the most complex geometry. They focused on the linear zone of lift, drag and moments curves, and pressure coefficient distributions. However, just a few participants were able to successfully predict the stall and the post-stall regions.[20] The slat tracks, flap track fairings and tubes bundle could partly be responsible for the stall entry; this fact highlights the importance of simulating the complete configuration to predict the stall.

3.2.2 Setup and mesh convergence

The geometry is based on the DLR F11. The study employs the Configuration 2 is formed by a wing (with deflected slat and flap, with 26.5deg and 32deg respectively) and fuselage. Configuration 5 is based in the Configuration 2 geometry including slat tracks, flap track fairings, and pressure tube bundles, as depicted in Figure 7. The reference area for dimensioning the aerodynamic coefficient is $S_{ref} = 0.41913\text{m}^2$ and the moment reference center is $x = 1.4289\text{m}$, $y = 0.0\text{m}$, and $z = -0.04161\text{m}$.
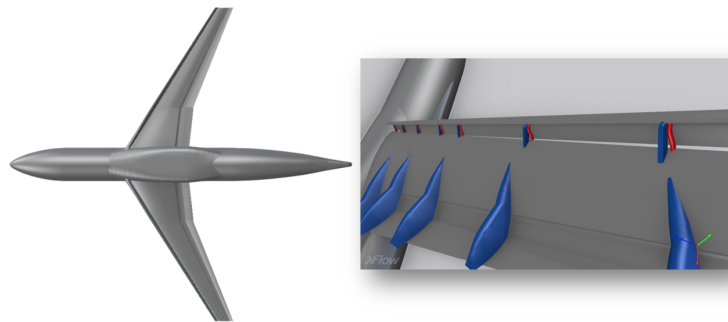

Figure 7: DLR F11 geometry for Configuration 2 (left) and Configuration 5 (right).[12]

The simulation setup is done in the XFlow environment, which features a virtual wind tunnel. The virtual wind tunnel is defined by a rectangular domain with pre-defined boundary conditions and is designed for external aerodynamics studies. The wind tunnel size is $(40, 20, 20)$m and is wide enough to avoid any wall effects. Its boundary conditions are set as an inlet velocity of 59.5 m/s which satisfies the Mach number condition of 0.175, and the outlet boundary is set as gauge pressure outlet of 0 Pa to model atmospheric conditions. The symmetry plane is set as a free-slip ground wall in order for the geometry to rely on it, and is an acceptable approximation for a symmetry plane.

Experimental data with two different flow conditions was provided by the HiLiftPW-2 committee. Two different Reynolds number were defined, $\text{Re} = 1.35 \cdot 10^6$ and $15.1 \cdot 10^6$ and Mach number was set to $\text{Ma} = 0.175$ for both flow conditions. The high Reynolds number condition ($\text{Re} = 15.1 \cdot 10^6$) results are going to be presented. The simulation is single-phase and isothermal since the regime is subsonic. The turbulence model used is the WALE viscosity model. The velocity field is initialized with the same magnitude and direction as the inlet velocity, and the initial gauge pressure field is set to 0 Pa within the entire fluid domain.

The study of grid convergence is a good practice in CFD and is necessary to determine the spatial discretization required to capture the physics of the problem. The HiLiftPW-2 committee provided coarse, medium, fine and extrafine meshes on which participants had to run their codes to check consistency and convergence of the solution. In contrast, XFlow avoids the traditional meshing process using an octree structure to address any complex geometry. A comparison is made for different sizes of near-wall refinements, with the farfield scale remaining fixed to 0.256 m, using the Configuration 2. Extra-coarse, coarse, medium, and fine resolutions are set as described in Table 2 at $\alpha = 16$deg. The criterion of solution convergence is based on the global lift and drag coefficients. It clearly shows that the solution becomes more accurate when the lattice is refined at the aircraft, especially for the extra-fine grid, which provides a good accuracy; the relative error of the lift prediction in comparison with wind tunnel tests is only 0.4% at 16 degrees. Nonetheless, the drag coefficient seems to converge with a lower number of elements.

INDUSTRIAL BENCHMARK SIMULATIONS OF DETACHED FLOWS USING XFLOW

Table 2: Resolution dependency study at 16deg.

Grid	Fuselage (mm)	Wing (mm)	Elements	Sim. time (s)	Cd	Cl	Comp. time (h)	Cores*
Extra-Coarse	4	4	$9.2 \cdot 10^6$	0.1	0.262	1.95	160	
Coarse	2	2	$25.9 \cdot 10^6$	0.1	0.295	2.16	5.2	160
Medium	1	1	$87.4 \cdot 10^6$	0.1	0.296	2.51	33.8	160
Fine	2	0.5	$150 \cdot 10^6$	0.1	0.310	2.67	84	256
Experimental	-	-	-	-	0.275	2.68	-	-

* CeSViMA: Supercomputing and Visualization Center of Madrid.

An important influence to the lattice resolution near walls is observed. However, the drag and lift variation seems within reasonable range and becomes reliable from 0.5mm wing resolution. The corresponding lattice structure (Fine resolution) provides a good accuracy with an acceptable computational time. Hence, it is the resolution employed for the rest of the study.

3.2.3 Results

In this section, the results obtained by XFlow and its comparison to experimental data for the full polar curve behavior at high Reynolds number conditions are presented. Figure 8.a shows the lift coefficient for both configurations which matches closely the experimental data below 16deg, in the linear zone where both absolute lift value and linear lift slope are successfully predicted. Indeed, the lift coefficient predicted for instance at 16deg by XFlow shows only 0.7% of relative error to wind-tunnel data, and the linear slope is exactly matched. Besides, it is observed the track fairings and pressure tube bundles have almost no effect on the aerodynamic coefficients in the linear zone. The difference appears in the stall region, where the stall angle of attack is predicted at 22.4deg in XFlow, instead of approximately 21deg according to the wind-tunnel data. Including the effect of the flap track fairings, slat tracks and slat pressure tube bundles, the coefficient seems to be more sensitive to these geometrical details in the stall region.
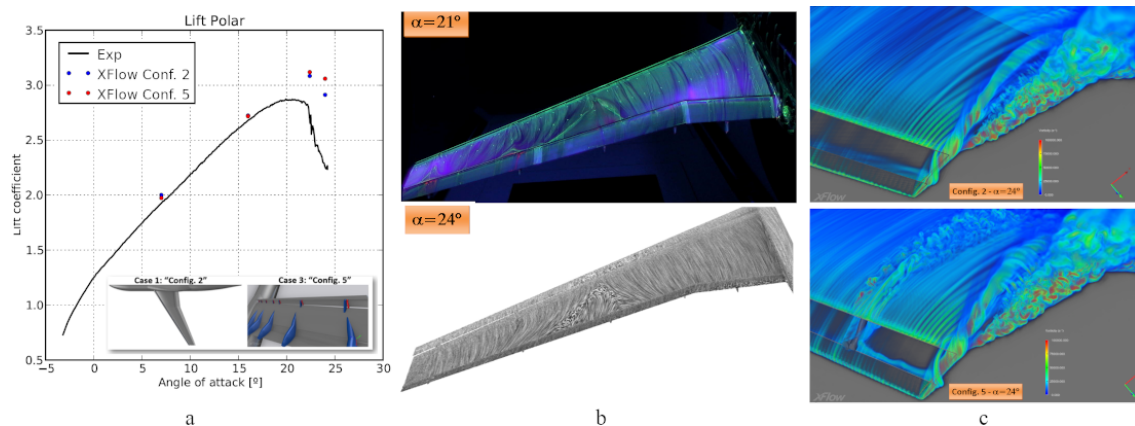

Figure 8: High-Lift aircraft configuration: (a) Lift and drag coefficients on conf. 2 and conf. 5 for Re= $15.1 \cdot 10^6$ (b) Flow pattern comparison between XFlow (bottom) and wind-tunnel oil flow images (top) for the stall region with conf. 5. (c) Volumetric rendering of vorticity comparison between Conf. 2 (top) and Conf. 5 (bottom) at 24deg.[12]

Additionally, XFlow predicts very well the experimental flow topology, as depicted in Figure 8.b, where the WMLES turbulence modeling can be appreciated. The flow structure at the wingtip 24deg with high Reynolds-number condition can be observed in Figure 8.c to compare the two configurations. One can appreciate the generation of the turbulent strips present for conf. 5; they are clearly induced by the slat tracks and the slat pressure tube bundles because this turbulent patterns does not show with conf. 2.

3.3 Dynamic stall: NACA0012

3.3.1 Introduction

The symmetric airfoil NACA0012 has been selected to validate XFlow when computing flows around moving geometries. The main aerodynamic differences between static and rotating lift curves are sketched in Figure 9. The dynamic stall

occurs when a rapid variation in the angle of attack is seen by the airfoil and typically leads to a hysteresis cycle in the aerodynamic forces. It is related to the apparition of a vortex near the leading edge on the suction side that enhances lift considerably (when compared to the static case). Massive and abrupt stall, linked to a sudden loss of lift, occurs once the vortex convects at the trailing edge. This phenomenon has been widely studied experimentally and numerically due to its appearance in helicopters aerodynamics and wind turbines.[3,7,15,18]

The variation of the angle of attack, α in the dynamic simulation is described by the following equation:

$$\alpha = \alpha_0 + \alpha_{\text{amp}} \sin \omega t \quad \text{with} \quad \omega = \frac{2U_\infty k}{c}, \tag{7}$$

where α_0 is the initial angle of attack, α_{amp} is the angle of attack amplitude, ω is the pitch rate, U_∞ is the reference velocity and k is the reduced frequency.
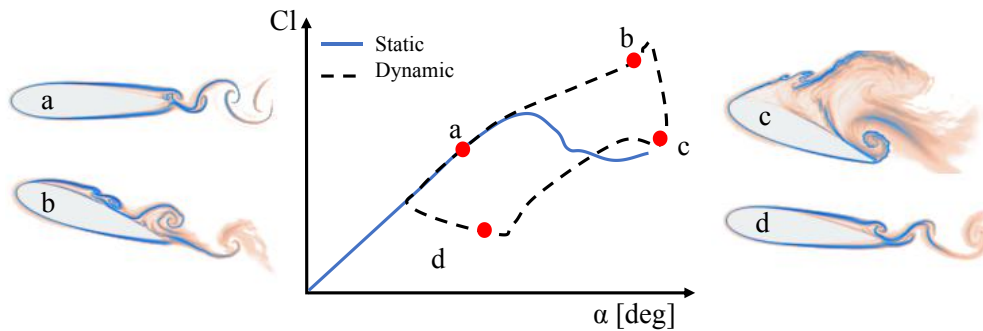

Figure 9: Dynamic stall phenomenon.

It is interesting to note that the pitch rate, ω, is directly governed by the non-dimensional reduced frequency, k. The reduced frequency governs the degree of unsteadiness such that for steady state aerodynamics $k = 0$, quasi-steady aerodynamics, $0 \le k \le 0.05$, and unsteady aerodynamics, $k > 0.05$. Additionally, for $k > 0.2$ it is considered highly unsteady aerodynamics.

In this study, a rotational velocity, $k = 0.1$ has been chosen to show the capability of XFlow to predict the dynamic stall. Lift, drag and pitching moment will be compared to experimental data.[15]

3.3.2 Setup and mesh convergence

The geometry for this study corresponds to the well-known NACA0012 airfoil. The reference chord length is $c = 0.61$m (or aerodynamic chord). The center of rotation is located at 25% of reference length, c, from the leading edge. These reference values are used to calculate the lift and drag coefficients and the pitching moment coefficient respectively.

A rectangular domain has been used with $32c$ long, $16c$ height and $2.5c$ wide. Farfield velocity boundary condition is used at the inlet and zero gauge pressure at the outlet. For the lateral walls have been used slip wall. At airfoil walls, non-equilibrium enhanced wall function is selected to take into account pressure gradients that may govern separation and stall. Additionally, the rotating geometry is addressed with immersed boundary method.

An external flow (single phase and air fluid properties) with the isothermal flow condition and the turbulence model, Wall-Adapting Local Eddy-viscosity (WALE). Where flow conditions are defined through the non-dimensional numbers: Mach number, Ma = 0.072, Reynolds number, Re = $0.98 \cdot 10^6$, and reduced frequency, $k = 0.1$.

In reference with the grid refinement, Figure 10 shows the grid convergence for different refinements (see Table 3). Figure 10 depicts the hysteresis for all lattice sizes. Additionally, we observe that for the finest mesh, the linear region and the maximum lift are well captured. Discrepancies can be seen in the low part of the curve, for all mesh sizes.

3.3.3 Results

In this section, the lift coefficient hysteresis and snapshots during the dynamic simulation with the Fine grid are shown in Figure 11. The lift coefficient has been compared with experimental[15] data and PowerFlow results.[18] PowerFlow is a commercial solver also based in the LBM.

XFlow captures well the maximum lift. The hysteresis is relatively well captured although discrepancies are observed in the recovery region. The instantaneous vorticity isocountours are depicted for various angles of attack which correspond to different points in the lift hysteresis loop: Note that, in the linear region, the flow is mainly attached

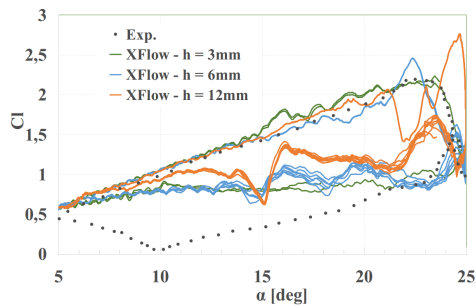INDUSTRIAL BENCHMARK SIMULATIONS OF DETACHED FLOWS USING XFLOW

Table 3: Resolution dependency at $\Delta P = 0$Pa.

	Lattice resolution (*mm*)	Elements	Simulation time (*s*)	Comp. time (*h*)	Cores *
Coarse	12	$0.3 \cdot 10^6$	2	3.8	8
Medium	6	$1.4 \cdot 10^6$	2	24.5	8
Fine	3	$9.5 \cdot 10^6$	2	100	40

* CeSViMA: Supercomputing and Visualization Center of Madrid.

Figure 10: Dynamic stall grid convergence.

(see Figure 11.a). In Figure 11.b the flow has detached and the convective vortex characteristic of rapid pitching (and dynamic stall) is near the end of the wing, which will soon produce an abrupt stall. The snapshots are consistent with the simulated and experimental curve. Figure 11.c is characterized by massive detachment and deep stall, the suction side of the wing shows indeed massive detachment. The lift coefficient in Figure 11.d and 11.e disagrees between computations and experiments. In these regions XFlow predict a more rapid recovery (less detachment) that in the experiments. Note that PowerFlow is able to obtain better results but still some discrepancies in the recover as detailed in Ribeiro and Casalino's work.[18]
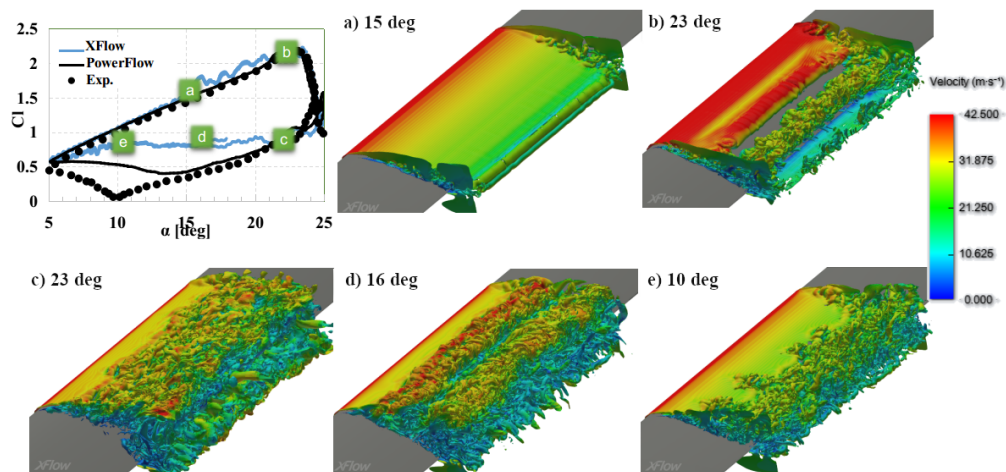
Figure 11: Dynamic stall for a NACA0012 airfoil: lift curve hysteresis (top-left) and 3D vorticity isosurface at different angles of attack, with Re=0.98 $\cdot 10^6$ and $k = 0.1$.

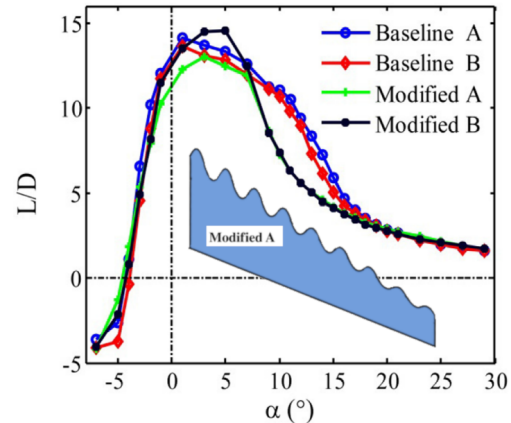## 3.4 Wing with leading-edge tubercles

3.4.1 Introduction

Tubercles have been proposed to soften aerodynamic characteristics near stall, the origin of this idea goes back to Humpback whale's fins[16] (see Figure 12), which have evolved during millions of years of evolution to enhance maneuverability in water. For example, an amazing feature of the humpback is its acrobatic behavior during feeding known as bubble netting. These whale's fins operate at Reynolds numbers, Re= $1.1 \cdot 10^6$, based on the sea water viscosity and density at 16 °C.

Tubercles are among other passive flow control devices, being explored to enhance aerodynamic performance. An overview of devices that may help control stall or improve performance (decrease drag) was summarized by Aftab et al.[1] The geometrical parameters that define the tubercles are the following:

- Wavelength, λ/c: defines the non-dimensional wavelength (or equivalently the spatial frequency) of the tubercles. Note that c is the local chord.

- Amplitude, A/c: defines the amplitude of the tubercles. It is also made non-dimensional using the local chord c.

- Span section, η/b: defines the wing span section where the tubercles start. Note that b is the total wing span.

Figure 12: Humpback whale's fins.[16]

Figure 13: Comparative aerodynamic efficiency of a wing with sweep-back with and without leading-edge tubercles.[13]

Aerodynamic characteristics at different Reynolds have been obtained in experiments. Johari et al.[13] tested a NACA63$_4$021 airfoil, at angle of attack range from 6deg to 30deg and Re $= 1.83 \cdot 10^5$ and $2 \cdot 10^6$. Airfoils with varying tubercle amplitude, $A = 0.025c, 0.05c$ and $0.12c$ and wavelength $\lambda = 0.25c$ and $0.5c$ were tested.[4] Forces and moments were measured in a water tunnel. The results showed smooth stall, due to the presence of the tubercles, improving the post-stall behaviour by 50%. Configurations with small amplitude, $A = 0.025c$, and large wavenumber $\lambda = 0.5c$ gave better results. Additionally, tubercles provide a reduction in performance in the pre-stall region but avoid the abrupt stall noticed for the baseline airfoil.

Later, Wei et al.[24] reported the differences between directing the tubercles normal to the span (modified A) or normal to the tapered leading edge (modified B). These also considered a tapered wing with sweep-back, with tubercles of amplitude, $A = 0.12c$, where c is the mean chord for rectangular wing and larger wavelength, $\lambda = 0.5c$. Similar resuts were obtained with these configurations (see Figure 13) where the post-stall behaviour improve, however the drag increased slightly.

In this section, a swept-wing is used to study the effect of the turbercules leading-edge in the aerodynamic properties.

3.4.2 Setup and mesh convergence

A swept-wing geometry has been used for this study. The analysis was performed using a baseline geometry, which was modified to include tubercles configurations. The mean aerodynamic chord and the wingspan are MAC = 2.702m and $b = 6.225$m respectively. The wing with leading-edge tubercles has been based on the baseline wing.

In this study, the tubercles have been varied to study their effect over the aerodynamic coefficients. The parametric study has been defined with the frequencies $\lambda/c = 0.1, 0.2$ and 0.4, and the amplitudes $A/c = 0.025, 0.05$ and 0.1. These values have been selected based on previous studies by Wei et al.,[24] who showed that for these values, the effect of the tubercles were more noticeable in this type of wing configuration. Table 4 shows the different set of parameter used to generate 9 different tubercles configurations. Additionally, the idea was to localize the tubercles only near the wing tip, since the baseline wing geometry was observed that stall initiates at the tip, in this study fixed to $\eta/b = 0.50$. Some configurations are shown in Figure 14.

The wind tunnel dimensions for the simulation are: $37c$ long, $9.25c$ wide and $18.5c$ height. The symmetry wall has been defined as free slip wall where the wing geometry relies on it. Velocity inlet boundary conditions are used at the inlet. Zero-gauge pressure is imposed at the outlet. Finally, the wing wall required the non-equilibrium enhanced wall functions to take into account pressure gradients.

The flow condition is defined by the Mach number which is set to Ma= 0.2 and the Reynolds number has been fixed to Re$/L = 4.66 \cdot 10^6$ with a reference length, L. The latter Mach and Reynolds correspond to see level conditions. Note that for each new geometry the surface area has been computed. This area is then used to non-dimensionalised the lift and drag forces, such that the resulting aerodynamic coefficients represent the relative force to the modified shape.

INDUSTRIAL BENCHMARK SIMULATIONS OF DETACHED FLOWS USING XFLOW

Table 4: Configurations of leading-edge tubercles

Baseline $\quad|\quad c = 2.702m \quad\quad b = 6.225m$

λ/c \ A/c	0.025	0.05	0.1
0.1	$A025\lambda10$	$A05\lambda10$	$A10\lambda10$
0.2	$A025\lambda20$	$A05\lambda20$	$A10\lambda20$
0.4	$A025\lambda40$	$A05\lambda40$	$A10\lambda40$

$A025\lambda10$ $\quad\quad\quad$ $A10\lambda10$

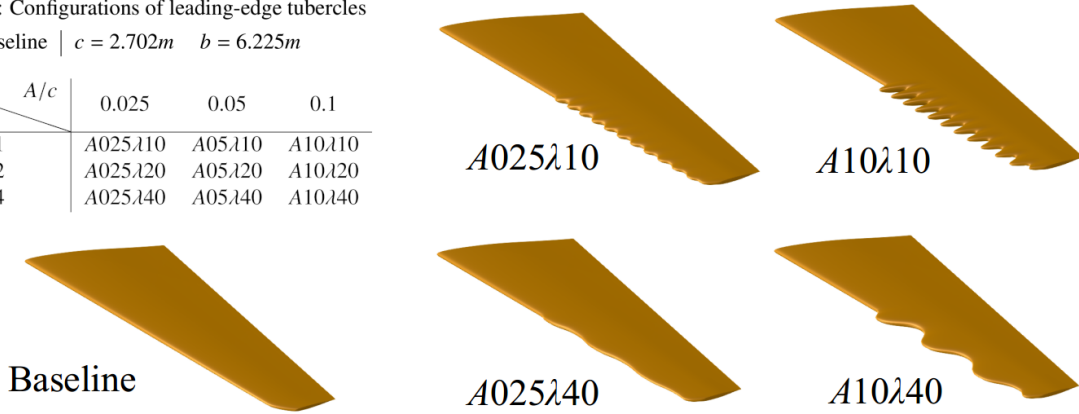Baseline $\quad\quad\quad$ $A025\lambda40$ $\quad\quad\quad$ $A10\lambda40$

Figure 14: Wing baseline and modified geometries.

An external flow (single phase and air fluid properties) with the isothermal flow condition and the turbulence model: Wall-Adapting Local Eddy-viscosity (WALE) have been selected.

The wing with $A/c = 0.025$ and $\lambda/c = 0.2$ has been used to study mesh convergence. For this purpose, we selected an angle of attack, $\alpha = 18deg$. It corresponds to the stall region in the lift curve (as will be shown later). To ensure that the mesh refinement does not affect the results, a comparison has been performed for different sizes of near wall refinements. In all cases the farfield scale is $5.12m$. Table 5 summarizes the lattice resolution, number of lattices in each grid, the drag and lift coefficients, the computational time and the number of cores used for computation. The 4 simulations use adaptive mesh refinement based on the vorticity field.

Table 5: Resolution dependency with configuration $A/c = 0.025$ and $\lambda/c = 0.2$ at $\alpha = 18deg$.

	Lattice resolution (mm)	Elements	Simulation time (s)	Cd	Cl	Comp. time (h)	Cores [*]
Extra Coarse	40	$3.3 \cdot 10^6$	3	0.254	0.780	19	8
Coarse	20	$4.2 \cdot 10^6$	3	0.242	0.872	28	8
Medium	10	$12.3 \cdot 10^6$	3	0.218	0.930	25	32
Fine	5	$42.0 \cdot 10^6$	3	0.215	0.941	155	32

[*] CeSViMA: Supercomputing and Visualization Center of Madrid.

Regarding the lift and drag coefficients in Table 5, it can be seen that the errors between both resolution 5 and 10mm are 1% for lift and 2% of drag. These convergence study is remarkable since at this angle of attack (with stalled flow), the flow is more complex to resolve. Looking for a trade-off between accuracy and computational cost, 10mm resolution has been used for the rest of simulations.

3.4.3 Results

First, a comparison between the different configuration have been computed. The results for lift, drag and efficiency at $\alpha = 18deg$ are compared in Table 6. The percentages, indicate the percentage variation of the modified geometry with respect to the baseline configuration. First, it can be seen that variations are relatively small in general. Second, we observe that the configurations $A10\lambda40$ and $A05\lambda40$ show a more important increase in the lift coefficient. The $A05\lambda40$ configuration shows an increase in the drag coefficient, however $A10\lambda40$ decreases the drag coefficient. This can be further quantified by comparing the lift over drag, L/D, where they have a 5.9% and 2.7% gain in L/D with respect to the baseline configuration. It may be concluded that $\lambda/c = 0.4$ is the wavelength that provides the more benefit, and that amplitudes around $A/c = 0.1$ show the most potential.

Having determined the most promising configuration for a high angle of attack ($\alpha = 18deg$), the rest angles of attack have been simulated as depicted Figure 15. The baseline geometry has been compared to the optimal tubercles configuration geometry ($A/c = 0.1$ and $\lambda/c = 0.4$). More interestingly, note that the geometries with tubercles show an identical lineal regime for low angle of attack and a higher maximum lift with a more benign stall. However, when comparing the drag, we observe a mild increase at medium range of angles of attack that results in a decrease of the

Table 6: Percentage variation of lift, drag and efficiency of the modified geometries (see Table 4) with respect to the baseline configuration.

	Baseline	$A10\lambda10$	$A05\lambda10$	$A025\lambda10$	$A10\lambda20$	$A05\lambda20$	$A025\lambda20$	$A10\lambda40$	$A05\lambda40$	$A025\lambda40$
% Cd	0	-8.3	-4.9	-3.5	-4.9	-2.6	-1.8	-1.7	2.8	-1.9
% Cl	0	-2.0	0.1	-1.7	0.4	0.0	0.1	4.1	5.5	0.8
% L/D	0	6.8	5.2	1.8	5.5	2.7	2.0	5.9	2.7	2.7

L/D. Overall, the efficiency, L/D, shows that the tubercles diminish the performance at medium range angles of attack, even if the lift coefficient improves near stall. These trends are remarkably similar to the experiments reported in Wei et al.[24] for a tapered swept-back wing, which was included in the introduction of this section (see Figure 13).
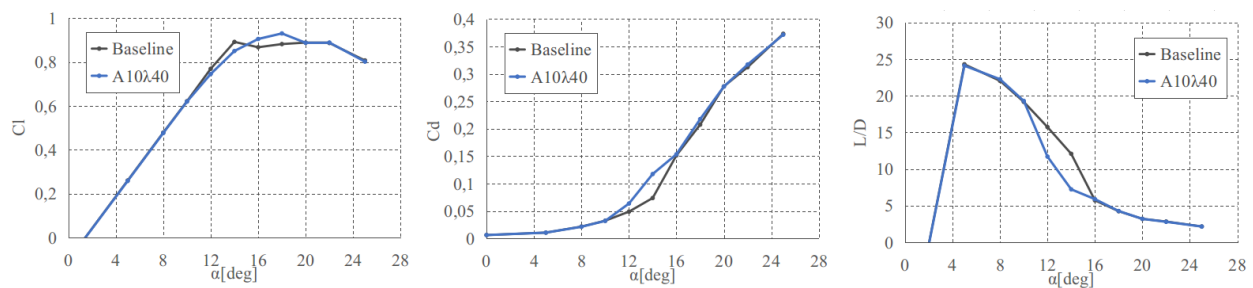
Figure 15: Lift and drag coefficient and aerodynamic efficiency for baseline and $A10\lambda40$ configuration geometries.

For completeness, Figure 16 includes visualization of instantaneous pressure contours on the wing surface for various angles of attack. The figures suggest that the higher lift at large angles of attack are related to localized suction regions, which are generated by the tubercles. These regions are particularly present at angles 12, 14 and 18deg and located near the wing tip. These results suggest that acting on the wing tip may have a beneficial effect on the aerodynamic performance, perhaps more important that including tubercles along 50% of the span.
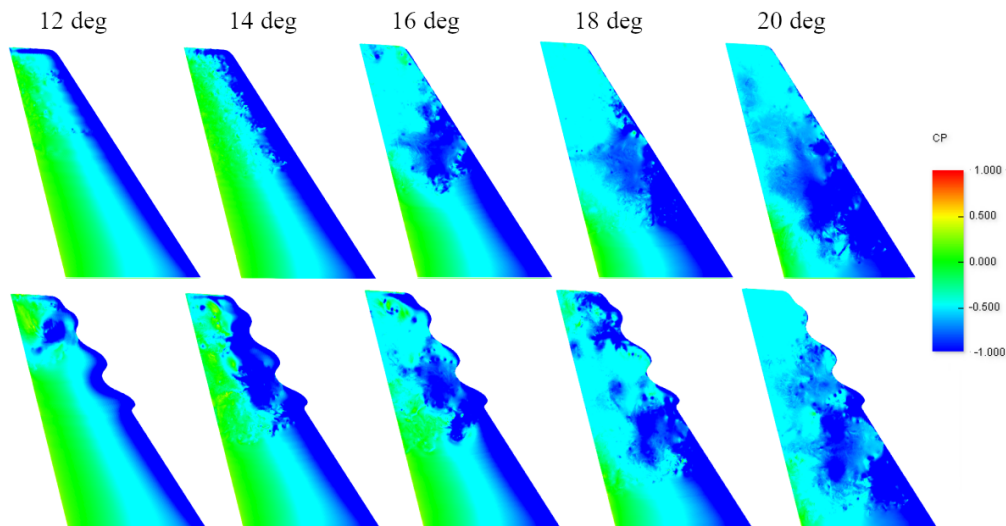
Figure 16: Surface pressure distribution for the baseline and $A10\lambda40$ configuration geometry at 12, 14, 16, 18 and 20 deg.

4. Conclusions

This work has shown that the lattice-Boltzmann method implemented in XFlow is able to solve advanced industrial problems even in the presence of complex geometries or moving parts. Four industrial cases have been studied, showing the reliability of the lattice-Boltzmann method to resolve detached flows in complex engineering problems.

The simple integration of a complete aircraft geometry at any angle of attack in XFlow made the setup simulation extremely short. The software demonstrated that it is able to solve an industrial problem of external aerodynamics on a detailed geometry using an automated lattice generation. This converts most of the engineer's efforts into machine efforts. The simulations were achieved in competitive turnaround time, especially given the unsteady and WMLES approach to predict with good accuracy detached flows. XFlow thus enables the study of the post-stall region even for very high angles of attack, where the flow becomes highly unsteady and turbulent with a minimum human factor and provides reasonable results.

5. Acknowledgments

References

[1] S.M.A. Aftab, N.A. Razak, A.S. Mohd Rafie, and K.A. Ahmad. Mimicking the humpback whale: An aerodynamic perspective. *Progress in Aerospace Sciences*, 84:48–69, 2016.

[2] Prabhu Lal Bhatnagar, Eugene P. Gross, and Max Krook. A model for collision processes in gases. I. small amplitude processes in charged and neutral one-component systems. *Physical review*, 94(3):511, 1954.

[3] Lawrence W. Carr. Progress in analysis and prediction of dynamic stall. *Journal of aircraft*, 25(1):6–17, 1988.

[4] Derrick S. Custodio. *The Effect of Humpback Whale-like Protuberances on Hydrofoil Performance*. PhD thesis, 2007.

[5] Dominique d'Humieres. Generalized lattice-Boltzmann equations. *Progress in Astronautics and Aeronautics*, 159:450–450, 1994.

[6] F. Ducros, F. Nicoud, and T. Poinsot. Wall-adapting local eddy-viscosity models for simulations in complex geometries, 1998.

[7] John A. Ekaterinaris and Max F. Platzer. Computational prediction of airfoil dynamic stall. *Progress in aerospace sciences*, 33(11-12):759–846, 1998.

[8] M. Geier, A. Greiner, and J.G. Korvink. A factorized central moment lattice Boltzmann method. *The European Physical Journal Special Topics*, 171(1):55–61, 2009.

[9] Martin Geier, Andreas Greiner, and Jan G. Korvink. Cascaded digital lattice Boltzmann automata for high Reynolds number flow. *Physical Review E*, 73(6):066705, 2006.

[10] Fabio R. Goldschmied. On the aerodynamic optimization of mini-rpv and small ga aircraft. In *American Institute of Aeronautics and Astronautics, Applied Aerodynamics Conference, 2 nd, Seattle, WA*, volume 21, 1984.

[11] Zhaoli Guo, Chuguang Zheng, and T.S. Zhao. A lattice BGK scheme with general propagation. *Journal of Scientific Computing*, 16(4):569–585, 2001.

[12] David M. Holman, Ruddy M. Brionnaud, Miguel Chávez-Modena Modena, and Eusebio Valero Sánchez. Lattice Boltzmann method contribution to the second high-lift prediction workshop. *Journal of Aircraft*, 52(4):1122–1135, 2015.

[13] Hamid Johari, Charles W Henoch, Derrick Custodio, and Alexandra Levshin. Effects of leading-edge protuberances on airfoil performance. *AIAA journal*, 45(11):2634–2642, 2007.

[14] Pierre Lallemand and Li-Shi Luo. Theory of the lattice Boltzmann method: Dispersion, dissipation, isotropy, galilean invariance, and stability. *Physical Review E*, 61(6):6546, 2000.

[15] William J. McCroskey, Kenneth W. McAlister, Laurence W. Carr, and S.L. Pucci. An experimental study of dynamic stall on advanced airfoil sections. volume 1. summary of the experiment. Technical report, NASA, 1982.

[16] D.S. Miklosovic, M.M. Murray, L.E. Howle, and F.E. Fish. Leading-edge tubercles delay stall on humpback whale (megaptera novaeangliae) flippers. *Physics of fluids*, 16(5):L39–L42, 2004.

[17] K.N. Premnath and S. Banerjee. On the three-dimensional central moment lattice Boltzmann method. *Journal of Statistical Physics*, pages 1–48, 2011.

[18] André F.P. Ribeiro, Damiano Casalino, and Ehab Fares. Lattice-Boltzmann simulations of an oscillating naca0012 airfoil in dynamic stall. In *Advances in Fluid-Structure Interaction*, pages 179–192. Springer, 2016.

[19] Ralf Rudnik, Kerstin Huber, and Stefan Melber-Wilkending. Eurolift test case description for the 2nd high lift prediction workshop. In *30th AIAA Applied Aerodynamics Conference*, page 2924, 2012.

[20] Christopher L. Rumsey and Jeffrey P. Slotnick. Overview and summary of the second aiaa high lift prediction workshop. In *52nd Aerospace Sciences Meeting*, page 0747, 2014.

[21] T.H. Shih, L.A. Povinelli, N.S. Liu, M.G. Potapczuk, and JL Lumley. A generalized wall function. *TM 113112 NASA Technical Report*, July 1999.

[22] Hendrik Tennekes and John Leask Lumley. *A first course in turbulence*. MIT press, 1972.

[23] Nicole M. Thomason. *Experimental investigation of suction slot geometry on a Goldschmied propulsor*. PhD thesis, 2012.

[24] Zhaoyu Wei, Tze How New, and Y.D. Cui. Aerodynamic performance and surface flow structures of leading-edge tubercled tapered swept-back wings. *AIAA Journal*, pages 423–431, 2017.